Salt permeation mechanisms in charge-patterned mosaic membranes

Journal:	*Molecular Systems Design & Engineering*
Manuscript ID	ME-ART-09-2018-000061.R1
Article Type:	Paper
Date Submitted by the Author:	28-Oct-2018
Complete List of Authors:	Summe, Mark; University of Notre Dame, Department of Chemical and Biomolecular Engineering Sahoo, Sushree Jagriti; Indian Institute of Technology Delhi Whitmer, Jonathan; University of Notre Dame, Chemical and Biomolecular Engineering Phillip, William; University of Notre Dame, Department of Chemical and Biomolecular Engineering

Design, System, Application: The selective transport of dissolved salts is critical to several membrane technologies that are necessary to meet the growing demand for water and energy; to support the development of therapeutic medicines; and to detect chemical and biological threats. Chemical patterning of charge- selective membranes permits exquisite control over the transport of specific solutes, either rejecting or facilitating the passage of dissolved salts based upon the surface chemistry of the membrane. Though these principles have existed for over eighty years, the lack of reliable manufacturing methods has obscured the molecular transport mechanism. Here, experiments using precisely engineered track-etched membranes and mathematical analysis that incorporates the structural charge inhomogeneity of charge patterned membranes elucidate the molecular processes underlying the rapid transport of salt through this class of membranes. Furthermore, the model presents a new tool to inform the design of charge-patterned membranes for optimal transport performance.

Salt permeation mechanisms in charge-patterned mosaic membranes

Mark J. Summe,[1] Sushree Jagriti Sahoo,[2] Jonathan K. Whitmer,[1] and William A. Phillip[1]

[1] *University of Notre Dame, Department of Chemical and Biomolecular Engineering, Notre Dame, IN 46556.*
[2] *Indian Institute of Technology Delhi, Department of Chemical Engineering, Delhi, India.*

Charge-patterned mosaic membranes contain channels of both positive and negative charge, creating a preference for the transport of whole salts to neutral solutes. In filtration processes, this unique property results in the enrichment of the salt concentration in the solution that permeates through the charge-patterned mosaic membrane. While this concept has been known since the pioneering work of Söllner, the lack of robust, repeatable manufacturing processes for generating chemically-patterned mosaic membranes has obscured the fundamental origins of this novel transport mechanism. Here, we utilize inkjet printing techniques to precisely pattern the pore wall chemistry of track-etched membranes and characterize them using diffusion cell experiments. Critically, the template-assisted inkjet printing method offers the advantage of a direct comparison between the well-understood case of single-charge membranes and charge-patterned membranes that were manufactured using the same ink formulations and printing methodology. Concomitantly, a model that adapts the constraint of Donnan equilibrium to account for the local variations in the electrical potential that arise near charge-patterned surfaces is developed to elucidate the pivotal role of patterning in determining the properties of the mosaic membranes. Experimentally, we observe that the salt permeability increases with concentration for the single-charge membranes, and decreases with concentration for the charge-patterned membrane. Strong quantitative agreement between the model and experiments implies that the local distribution of ions within the double layer, and its effects on ion partitioning, results in the emergence of distinct transport properties when charged elements are patterned on a substrate.

Design, System, Application: The selective transport of dissolved salts is critical to several membrane technologies that are necessary to meet the growing demand for water and energy; to support the development of therapeutic medicines; and to detect chemical and biological threats. Chemical patterning of charge-selective membranes permits exquisite control over the transport of specific solutes, either rejecting or facilitating the passage of dissolved salts based upon the surface chemistry of the membrane. Though these principles have existed for over eighty years, the lack of reliable manufacturing methods has obscured the molecular transport mechanism. Here, experiments using precisely engineered track-etched membranes and mathematical analysis that incorporates the structural charge inhomogeneity of charge-patterned membranes elucidate the molecular processes underlying the rapid transport of salt through this class of membranes. Furthermore, the model presents a new tool to inform the design of charge-patterned membranes for optimal transport performance.

I. INTRODUCTION

Membrane technologies are used ubiquitously to selectively control molecular transport, preferentially separating valuable or harmful species from source streams. State-of-the-art membranes typically mediate mass transfer using size selective mechanisms, and recent advances in nanostructured materials are pushing these mechanisms to their physical limitations [1, 2]. The fundamental limitations of size-selectivity have catalyzed interest in methods to tailor the surface chemistry of membranes [3–6] and imbue them with molecular controls for mass transfer. Newly proposed materials have demonstrated the ability to adsorb target solutes [7–10], catalyze reactions [11, 12], alter permeability in response to external stimuli [13], and selectively transport target species [14, 15]. However, membranes based on these materials typically require the majority of the solution to transport through the membrane. In some applications, such as wastewater reuse [16], resource recovery [17], chiral separations [18], and sensing [19], where the target solutes are present at dilute concentrations, this approach is inefficient as it is preferred to enhance the transport of the dilute molecules. In this regard, patterning the surface chemistry of membranes has great potential because it can result in the preferential transport of target molecules relative to solvent molecules.

Membranes with a single type of fixed surface charge (*e.g.*, ion exchange membranes and nanofiltration membranes) have been a subject of intense scrutiny [20–23] that has identified the fundamental mechanisms enabling the selective transport of counter-ions over co-ions [24–26]. While essential phenomena regarding selective ion transport through single-charge membranes are not sufficiently understood, general frameworks exist for understanding and engineering properties of these membranes [14, 27]. Patterned membranes are not simply a sum of these single-charge parts. When an array of oppositely-charged elements are patterned on a single membrane, altogether new properties emerge that are distinct from the single-charge limits [28, 29]. In nanofiltration processes, where pressure-driven flows mediate the ion-solvent separation, the concentration of salt

in the solution that permeates through a single-charge membrane is reduced relative to the concentration of the feed solution. Though the membrane's charge increases the concentration of counter-ions locally, reduced concentrations of co-ions and electroneutrality restrictions ultimately result in salt rejection [30–32]. Conversely, in filtration experiments, the charge-patterned structures of mosaic membranes can enhance the concentration of both ion species within the membrane pores, resulting in enriched salt concentrations in the efflux from the membrane [33]. This ability to separate and concentrate target salts in the efflux can offer advantages in the separation of dilute ionic solutes where existing processes such as electrodialysis struggle. However, to realize this potential application the molecular principles underlying salt enrichment must be identified.

The concept of charge-patterned mosaic membranes is not new, though principles for precise control over their fabrication have emerged only recently. In the 1930's, Karl Söllner postulated [34] and later demonstrated [35] that an array of negatively-charged and postively-charged elements utilized within a closed-loop device could engender the rapid and selective transport of dissolved salts. His design inspired the development of charge mosaic membranes featuring discrete positively- and negatively- charged domains arranged on a single substrate. Since these initial developments, charge mosaic membranes have been fabricated from electrospun polymers [36], copolymers [37, 38], ion exchange resins [39–41], polymer blends [42, 43], and polymeric nanotubes [44]. However, the development and proliferation of mosaic membranes stalled due to difficulties associated with precisely generating charge patterns [45]. Critically, the lack of a reliable method for producing mosaic membranes has made it difficult to understand the fundamental mechanisms underlying the membranes' function in a manner that ultimately allows them to be engineered for optimal salt transport.

Recently, a facile method leveraging inkjet printing was shown to successfully overcome many of the inherent design challenges in the repeatable, large-scale patterning of membrane chemistries [33, 46]. This technique prints polymer composite inks onto nanoporous substrates, coating the surface of the porous substrate and the interior of pores to create high affinity domains for both cations *and* anions of a given salt. Importantly, the rational design of the polymer composite inks makes it possible to independently formulate positively-charged, negatively-charged, and uncharged inks that can be utilized to create a family of uncharged, single-charge, and charge-patterned membranes having identical nanostructure yet variable chemistry. In particular, this allows the direct comparison of transport through single-charge and mosaic membranes, controlling for variability in substrate nanostructure and membrane fabrication. Here, using a combination of experiments enabled by inkjet printing and a new theoretical description for mosaic membranes that reconciles Donnan equilibrium with the local variations in electrostatic potential within the double layer, we develop a holistic understanding of salt transport through chemically-patterned charge mosaic membranes enabling future optimization and engineering of the membrane properties.

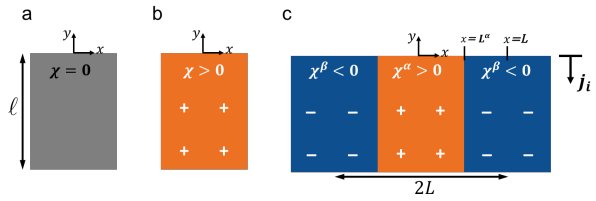

FIG. 1. Schematics of the three types of membranes examined in this study: (a) no surface charge, (b) single surface charge, and (c) a charge-patterned mosaic consisting of alternating positively- and negatively-charged stripes. The concentration of fixed charge is given by χ. The x-axis is along the surface of the membrane, while the y-axis moves from the surface into the solution. As indicated by the direction of the associated arrow, the flux j_i of species i is from the upstream to the downstream, which are positioned at the top and bottom of the schematic, respectively. ℓ is the membrane thickness and L is the width of the stripes that constitute the pattern of the charge mosaic membrane. The widths of the oppositely-charged stripes are assumed to be equal. Therefore, with $x = 0$ defined to be in the middle of the positive domain, to make use of the symmetry and periodicity of the pattern, the interface between the two differently charged domains is located at $x = L^{\alpha} = \frac{L}{2}$.

II. THEORY

We present a model for the transport of equivalent salts through the charge-patterned membranes that captures the variations in salt permeability observed in experiments. Critically, it must reduce to the established limits of salt transport through an uncharged membrane and salt transport through a single-charge membrane. Fig. 1 specifies the coordinate system and key characteristics for the three types of membranes: (a) no surface charge, (b) single surface charge (positive, without loss of generality), and (c) a charge-patterned mosaic. Salt transport through these membranes depends critically on phenomena occurring both within the membrane volume and at the solution-membrane interfaces. The upstream interface imposes a change in the free energy landscape that ions must navigate to partition into the membrane. Subsequently, ions diffuse across the length of the membrane before partitioning into the downstream reservoir. The salt flux will be calculated by integrating the ion fluxes over the membrane thickness after accounting for the spatial variation in the ion concentrations at the interfaces.

A. Molar Flux of Salts

The pores in the nanostructured substrates traverse the membrane without intersecting and the membrane is thick relative to the microscopic length-scales of the problem (*e.g.*, pore diameters, the Bjerrum length λ_B, and Debye length λ_D). Hence, we assert that the electroneutrality constraint may be applied within a volume V enclosing the membrane and extending a few λ_D from the surface, implying

$$\int_V \left(\sum_i^{1,2} z_i c_i(\vec{r}) + \chi(\vec{r}) \right) d\vec{r} = 0 \tag{1}$$

where z_i and c_i are the charge and the concentration of the ions, respectively. A subscript i of 1 denotes the cation and a subscript i of 2 denotes the anion. The term $\chi(\vec{r})$ represents the charge density due to fixed groups within the membrane, which are assumed to be uniformly distributed over the thickness, ℓ. This fixed charge must be balanced within the membrane by absorbing counter-ions from the bulk solution. For uncharged membranes [Fig. 1(a)], $\chi = 0$, while for charged membranes [Figs. 1(b,c)], χ is finite and depends on the chosen surface chemistry (*e.g.*, $\chi > 0$ for positively-charged membranes). For charge-patterned membranes, $\chi(\vec{r})$ is a function of position in the x-direction. By assuming electroneutrality within the volume V, microscopic charge imbalances in the system, and the resulting electric fields, are confined to thin regions at the solution-membrane interface. Thus, their primary effect is to skew the concentrations of ions available for transport through the membrane. We contend that such ion partitioning is crucial in determining the behavior of a mosaic membrane.

In the case of the diffusion cell experiments, convective transport is negligible, so the resulting Nernst–Planck relation for molar flux is

$$\vec{j}_i(\vec{r}) = -D_i \left(\nabla c_i(\vec{r}) + \frac{z_i \mathcal{F} c_i(\vec{r})}{RT} \nabla \phi(\vec{r}) \right) \tag{2}$$

where D_i is the ion's diffusion coefficient, $\mathcal{F}$ is the Faraday constant, R the gas constant, T temperature, and ϕ is the total electrostatic potential. Because no external potential is applied across the membranes in the experiments, the net ionic current through the membrane can be assumed to be zero.

$$\vec{I} = \sum_i^{1,2} z_i \mathcal{F} \vec{j}_i(\vec{r}) = 0 \; . \tag{3}$$

This constraint enables Eqs. 2 and 3 to be solved for the diffusion potential and subsequently the molar flux of each ion. Here, it is be assumed that the solute of interest is a symmetric salt where $z_1 = -z_2 = z$. Under these conditions, the flux through a charged membrane satisfies (see *Electronic Supplementary Information (ESI)* for a derivation)

$$\vec{j}_1(\vec{r}) = -D_1 D_2 \left[\frac{2c_1(\vec{r}) + \frac{\chi(\vec{r})}{z}}{(D_1 + D_2)\, c_1(\vec{r}) + \frac{D_2 \chi(\vec{r})}{z}} \right] \nabla c_1(\vec{r}) \tag{4}$$

The walls of the track-etched substrates are impermeable, thus the transport of salt between upstream and downstream reservoirs is governed by the y component of the flux. Hence, $\vec{j}_i = j_i \hat{y}$ and $\nabla \phi = \frac{d\phi}{dy} \hat{y}$. We may then substitute the appropriate form of $\chi(\vec{r})$ into Eq. 4 to obtain the flux for each membrane. In practice, χ is seen to have minor influence in this expression, so that under the relatively mild assumption that $D_1 = D_2$, expressions for ion flux effectively reduce to

$$j_1(x) = -D_1 D_2 \left(\frac{2}{D_1 + D_2} \right) \frac{dc_1(x)}{dy} \; . \tag{5}$$

Including the effects of χ in molar flux calculations provides an $\approx 2\%$ correction in our systems of interest. Thus, what is most important is the concentration $c_1(x)$ from which the gradient and flux are then determined. Eq. 5 can then be integrated over the membrane thickness to express the instantaneous flux of ions as a function of the concentration difference across the membrane. What remains to complete this model is a careful accounting of ion partitioning at the interface [20, 47–50].

B. Partitioning of Ions

The electrochemical potential μ_i of ions varies continuously across solution-membrane boundaries. The value on the membrane side, μ_i^m, is equal to the the value on the solution side, μ_i^s, at all points $\vec{r}$ within the interface,

$$\mu_i^0 + RT \ln c_i^m(\vec{r}) + z_i \mathcal{F} \phi^m(\vec{r}) = \mu_i^0 + RT \ln c_i^s(\vec{r}) + z_i \mathcal{F} \phi^s(\vec{r}) \; . \tag{6}$$

This relationship, satisfied at both the upstream and downstream interfaces, may be rearranged to relate the electrostatic potential to variations in ion concentration [47]

$$\phi^m(\vec{r}) - \phi^s(\vec{r}) = \frac{RT}{z_i \mathcal{F}} \ln \frac{c_i^s(\vec{r})}{c_i^m(\vec{r})} \; . \tag{7}$$

Here, the solutions are assumed to be ideal. This assumption breaks down at high salt concentrations [14, 20, 21, 23, 25, 27, 51, 52]. For the charge-patterned membranes, deviations from ideality will not qualitatively alter the behaviors seen in ion partitioning, and thus make sense to treat after the effects of charge heterogeneity are considered. We thus leave non-ideal solution effects as a subject for future investigation. Equating the expressions for $\phi^m(\vec{r}) - \phi^s(\vec{r})$ based on the concentration of anions and concentrations of cations results in the Donnan equilibrium condition. For symmetric salts [47],

$$c_1^m(\vec{r}) c_2^m(\vec{r}) = c_1^s(\vec{r}) c_2^s(\vec{r}) = c_b^2 \tag{8}$$

where c_b is the concentration of salt in solution. For the uncharged membrane, Eqs. 1 and 8 imply

$$c_i^m = c_i^s = c_b \ . \tag{9}$$

For single-charge membranes, the standard derivation of Donnan equilibrium assumes that electroneutrality holds locally at all positions, which implies a discontinuous jump in potential at the solution-membrane interface. This is not representative of the microscopic physics, though it approximates the behavior when viewed on scales much larger than λ_{D}. In this view, Eqs. 1 and 8 can be used to express the concentrations of co- and counter-ions, respectively, within the membrane as a function of the salt concentration in solution,

$$c_1^m = \frac{-\chi + \sqrt{\chi^2 + 4c_b^2}}{2} \ , \quad c_2^m = \frac{\chi + \sqrt{\chi^2 + 4c_b^2}}{2} \ . \tag{10}$$

The strong local electroneutrality assumption can be relaxed by solving the Poisson–Boltzmann equation near the interface [53]. In this approach, the value of $\phi^m(\vec{r}) - \phi^s(\vec{r})$ varies smoothly over the double layer. As a result, the concentration of counter-ions from the dissolved salt increases from its bulk value, to an enriched value within the membrane. As the total excess of charge contained within the double layer balances the fixed charge on the membrane, and inhomogeneities are confined within a few λ_{D} of the interface, Eq. 10 still describes ion partitioning for thick membranes like those examined here [53].

In the case of a charge-patterned membrane, the electrostatic potential varies laterally within the plane of the interface. Donnan equilibrium still holds locally, but the assumption that electroneutrality is maintained locally by dissolved ions is no longer valid. Instead, the oppositely-charged portions of the membrane can also interact with each other. As such, the local variations in potential must be modified to account for these interactions in the case of alternating charged domains on the membrane surface. We therefore solve the Poisson–Boltzmann equation in the Debye–Hückel limit under the assumption that the y dependence of c_i is confined to the solution side of the interface [53]. For a membrane patterned with alternating stripes of equal width, ϕ is given by the following differential equation:

$$\frac{\partial^2 \phi}{\partial x^2} + \frac{\partial^2 \phi}{\partial y^2} = \frac{\phi}{\lambda_D^2} \ , \tag{11}$$

together with periodic boundary conditions in x on ϕ and $\frac{d\phi}{dx}$ as well as

$$\begin{aligned} \lim_{y\to\infty} \phi &= 0 \\ -\frac{d\phi}{dy}\Big|_{y=0} &= \begin{cases} \frac{-\sigma_0}{\epsilon} & \frac{L}{2} < |x| < L \\ \frac{\sigma_0}{\epsilon} & |x| < \frac{L}{2} \end{cases} \ . \end{aligned} \tag{12}$$

Solving this system [54] yields

$$\phi = \sum_{n=0}^{\infty} \frac{4\sigma_0 \sin\left(\frac{n\pi}{2}\right)}{n\pi\epsilon\sqrt{\left(\frac{n\pi}{L}\right)^2 + \frac{1}{\lambda_D}^2}} \cos\left(\frac{n\pi x}{L}\right) \exp\left(-\left(\left(\frac{n\pi}{L}\right)^2 + \frac{1}{\lambda_D^2}\right)^{\frac{1}{2}} y\right) \tag{13}$$

where σ_0, ϵ, and L are the areal surface charge density (proportional to χ), permittivity, and stripe width, respectively. Taking the potential in the bulk solution ϕ^s to be a reference value of 0, $\phi^m(\vec{r}) - \phi^s(\vec{r})$ can be evaluated from the solution of Eq. 13 at the surface of the membrane, $y = 0$. Subsequently, the partitioning of ions at the solution-membrane boundary can be determined by averaging Eq. 7 over one full pattern

$$c_i^m = \frac{1}{2L} c_b \int_{-L}^{L} \exp\left(\frac{-z_i \mathcal{F} \phi(x, y=0)}{RT}\right) dx \ . \tag{14}$$

Eqs. 9, 10 and 14 predict the uptake of ions within the membranes as a function of c_b (Fig. 2a and 2b). These can be utilized as boundary conditions that allow Eq. 5, to be integrated, and j_1 to be expressed as a function of the salt concentration in the upstream reservoir. If deionized water is utilized in the downstream reservoir, this concentration may be taken to be zero. Utilizing the constraint of zero net ionic current we may then obtain the salt flux $j_s = j_1 = j_2$ for each of the membranes.

Normalizing the salt fluxes by the driving force for permeation based on the concentrations in solution yields expressions for the permeabilities, *i.e.*, $P \equiv \frac{j_s \ell}{\Delta c_b}$. The variations of permeability with the upstream salt concentration predicted by this analysis are shown in Fig. 2c. Most notable is the divergence of j_s versus concentration for the single-charge membrane compared to the charge-patterned mosaic membrane. It is these trends in permeability as a function of concentration that were examined experimentally.

III. EXPERIMENTAL

A. Materials

Polycarbonate track-etched (PCTE) membranes (pore diameter: 50 nm; thickness: 10 µm; porosity: 0.6%) were purchased from Whatman. Poly(vinyl alcohol) (PVA, 89-98 kDa; 99+% hydrolyzed),

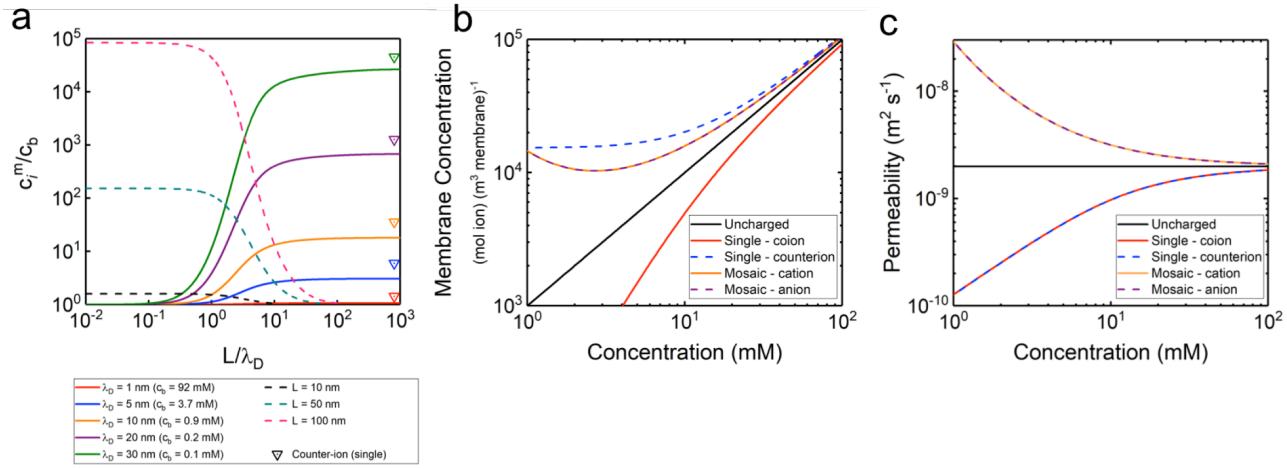

FIG. 2. (a) Partitioning of cations and anions in a charge-patterned mosaic membrane as a function of the stripe width L and Debye length λ_D. c_i^m and c_b are the concentrations in the membrane and the bulk of the upstream solution, respectively. Solid lines hold λ_D constant while varying L; dashed lines hold L constant while varying λ_D. The triangle markers represent the partitioning of counter-ions in a single-charge membrane at the same values of λ_D. (b) Partitioning of ions into the three types of membranes plotted as a function of salt concentration. The black line represents ion uptake (Eq. 9) by a membrane with no surface charge. The solid red and dashed blue lines model co-ion and counter-ion, respectively, uptake (Eq. 10) by a membrane with a uniform surface charge. The purple and orange lines model ion uptake (Eq. 14) by a charge-patterned mosaic membrane, *i.e.* a membrane with alternating domains of positive and negative charge. (c) The permeability of ions through the three types of membranes plotted as a function of upstream salt concentration. The black line represents salt permeability through a membrane with no surface charge. The solid red and dashed blue lines model co-ion and counter-ion permeability, respectively, through a membrane with a uniform surface charge. The purple and orange lines model ion transport through a charge-patterned mosaic membrane.

poly(diallyldimethylammonium chloride) (PDADMAC, M_W < 100 kDa), poly(styrene sulfonate) (PSS, 70 kDa), poly(ethylene oxide) (PEO, 35 kDa), KCl, K_2SO_4, $MgCl_2$, $MgSO_4$, hydrochloric acid (37 wt%), and glutaraldehyde (25 wt%) were purchased from Sigma Aldrich. Acrodisc syringe filters with 1 µm glass fiber were purchased from the Pall Corporation. All materials were used as received. 18.2 MΩ DI water was obtained from an EMD Millipore water purification system.

B. Polymer Composite Ink Solutions

Preparation of composite inks and printing of membranes was reported previously.[33] A 0.75 wt% PVA solution was first prepared by dissolving an appropriate amount of the PVA powder in DI water while heating the mixture to 80 °C for 2 h. Subsequently, the functional component was dissolved in the PVA solution to form the composite ink. The functional component was either 0.1 M PDADMAC, 0.5 M PSS (based on the repeat unit molecular weights), or 2 wt% PEO. Composite inks were then filtered through the Acrodisc syringes to ensure that no particulates would clog the print heads.

C. Membrane Printing Procedure

All membranes were printed using a Jetlab 4 xl-A system (MicroFab Technologies) equipped with 50 µm print heads. A PCTE membrane was placed onto a home-built vacuum device, and composite inks were printed onto the membrane while pulling vacuum of 12 psiv to facilitate the transport of inks into the pores of the membrane. Each membrane was printed using 5 overprints, defined as the number of times the print head deposits an ink droplet at the same location. To form a continuous stripe, droplets were ejected from the print head every 80 µm, which is the approximate diameter of the ejected droplets of ink.

Single-charge and uncharged membranes were printed with only one composite ink: PDADMAC/PVA for cationic, PSS/PVA for anionic, and PEO/PVA for uncharged. Charge-patterned mosaic membranes were printed with alternating stripes of PDADMAC/PVA and PSS/PVA composite inks. The width of each stripe was 100 µm. This approach resulted in charge-patterned membrane surfaces with roughly 50% positive coverage and 50% negative coverage.

D. Chemical Cross-linking of Printed Membranes

To ensure the functional components of the membranes did not dissolve in subsequent tests, the membranes were chemically-crosslinked using hydrochloric acid and glutaraldehyde vapors. After depositing the composite ink(s), the membranes were placed in a closed glass chamber containing two beakers: one filled with 20 mL of hydrochloric acid and the other containing 20 mL of glutaraldehyde. The glass chamber sat on a hot plate that was set at 45 °C for 24 h. Upon completion, membranes were rinsed in DI water three times for 1 h and dried in air for storage between experiments.

E. Diffusion Experiments

Salt transport through uncharged, single-charge, and charge-patterned mosaic membranes was studied using diffusion cell experiments. In the diffusion cell apparatus (*ESI*, Fig. S1), a membrane was placed between two reservoirs: an upstream reservoir that contained an aqueous solution of a single salt at a known concentration and a downstream reservoir that contained deionized water. A negligible amount of water passed through the membrane while salt was transported between the upstream and downstream reservoirs. The resulting concentration difference between the two reservoirs was monitored over time (t) and plotted as $\ln(\Delta c(0)/\Delta c(t))$. This yields a straight line whose slope is proportional to the salt permeability, P [55]. In this manner, the permeability values for KCl, K_2SO_4, $MgCl_2$, and $MgSO_4$ were obtained as a function of the salt concentration in the upstream reservoir. Details regarding the quantification of the salt concentrations are reported in the *Electronic Supplementary Information*.

IV. RESULTS AND DISCUSSION

Three classes of membranes: uncharged, single surface charge, and charge-patterned mosaics were generated by printing polymer composite inks onto nanoporous polycarbonate track-etched (PCTE) substrates. Uncharged membranes were prepared by printing a poly(ethylene oxide)/poly(vinyl alcohol) (PEO/PVA) composite ink onto the PCTE substrate. PEO, an uncharged polymer, was utilized to produce membranes with a similar pore size as membranes fabricated with inks containing polyelectrolyte components but without imprinting a surface charge. Two types of single-charge membranes were prepared, anionic membranes and cationic membranes, using a negatively-charged poly(styrene sulfonate)/poly(vinyl alcohol) (PSS/PVA) composite ink or a positively-charged poly(diallyldimethylammonium chloride)/poly(vinyl alcohol) (PDADMAC/PVA) composite ink, respectively. Charge-patterned mosaic membranes were prepared by printing alternating 100 µm-wide stripes of the PSS/PVA and PDADMAC/PVA composite inks, producing patterned membranes that were charged locally at the length scale of the pattern but were overall net neutral.

Prior studies on charge-patterned membranes have predominantly used pressure-driven filtration experiments to examine transport. In particular, the observation of salt enrichment was taken as an indicator of the successful formation of the mosaic membrane archetype. However, these filtration experiments introduce complexities because convection dominates transport and there are multiple phenomena that can lead to salt enrichment [30, 52]. Diffusion cell experiments mitigate the influence of these factors. A representative set of results from the diffusion cell experiments, executed using anionic membranes and 10 mM feed solutions, are plotted in Fig. 3(a). The results from two distinct membrane samples are presented as the set of solid lines and the set of dashed lines. The four salts studied (KCl, K_2SO_4, $MgCl_2$, $MgSO_4$) were utilized due to their varying valency. For the negatively-charged, anionic membrane, $\ln(\Delta c(0)/\Delta c(t))$ increases most rapidly with time for $MgCl_2$ and most slowly for K_2SO_4, which implies that $MgCl_2$ has the highest permeability, while K_2SO_4 has the lowest. Permeabilities obtained from these experiments are compiled in Fig. 3b.

Salt permeabilities for uncharged membranes demonstrate small variations in magnitude relative to each other, which is consistent with the value of the diffusion coefficients of these salts in water (*ESI*, Figs. S2–S3) [55]. Furthermore, these permeabilities are consistent with the value of the diffusion coefficients reduced by a factor proportionate to the porosity of the modified PCTE substrates (0.2-0.3%, *ESI*, Fig. S4). This trend indicates that the nanostructure of the inkjet printed membranes reduces the area available for permeation, but does not otherwise alter the diffusion of salt.

The introduction of charged inks had a marked effect on the permeability of the membranes. Each charged membrane has one salt with a noticeably higher permeability value relative to the permeability values of the other salts for that given membrane. Concomitantly, these permeability values are larger than the values for all four salts through the uncharged membrane, indicative of the strong influence of charge on transport. For both single-charge membranes, the asymmetric salt with the divalent counter-ion has the highest permeability while the salt with a divalent co-ion has the lowest permeability, similar to trends observed in ion exchange membranes [25, 27]. This trend emerges because counter-ions are electrostatically attracted at the double layer [56] while co-ions are electrostatically repelled [20, 47]. The results shown in Fig. 2b reiterate these findings for the single-charge membranes. In particular, the high concentration of counter-ions absorbed through the solution-membrane interface is necessary to balance the fixed surface charges, while the co-ion concentration is significantly depleted. In the absence of an external field, the

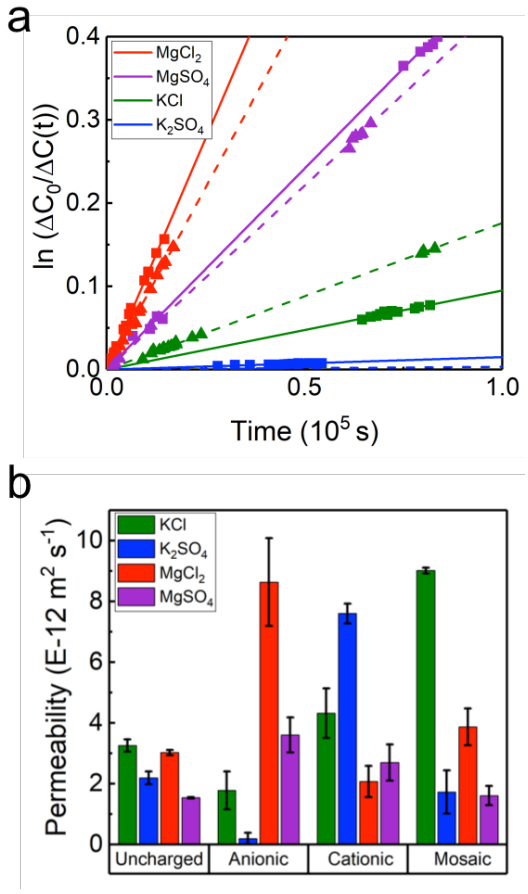

FIG. 3. (a) Representative results from diffusion cell experiments. The reported data were obtained using negatively-charged (*i.e.*, anionic) membranes and single salt upstream solutions with the salt dissolved at a concentration of 10 mM. Four salts and two membranes were used in the collection of the reported data. Salt identity is indicated by color as shown in the legend. The solid lines correspond to the data obtained from one membrane sample and the dashed lines indicate results from a second membrane sample. The slope of the line is proportional to the permeability of the salt through the membrane. (b) Average permeability values calculated from diffusion cell experiments. All experiments were performed using a 10 mM upstream salt concentration. Experiments were conducted on a series of four different membranes. Membranes with no surface charge (uncharged), membranes with a negatively-charged surface (anionic), membranes with a positively-charged surface (cationic), and membranes with charge-patterned surfaces (mosaic). Error bars represent one standard deviation from the mean taken from at least three membranes.

counter-ion cannot permeate through the membrane independently without violating electroneutrality. As such, it is the repulsion of co-ions that limits the salt throughput (*i.e.*, Donnan exclusion). The higher charge of the divalent ions either exacerbates the repulsion of the co-ions or increases counter-ion sorption relative to the weaker repulsion of the co-ion [38, 57]. For the membranes examined here, the anionic membranes appear to be better at excluding divalent co-ions than the cationic membranes, which is likely due to the small difference in the magnitude of their surface charges (*ESI*, Fig. S5).

Experiments and theoretical results are thus in agreement with prior well-established results for single-charge ion exchange membranes. Importantly, in the context of the current study, these experimental results confirm the viability of producing ion exchange membranes via printing. As such, the properties of charge-patterned mosaics can be contrasted directly with the ion exchange elements that comprise them. This capability is critical to understanding the mosaic membranes, as PSS/PVA and PDADMAC/PVA chemistries patterned onto a single substrate result in altogether different transport. It is the symmetric, monovalent salt, KCl, that has the highest permeability, significantly higher than any of the salts in an uncharged membrane (Fig. 3b).

Printing equal areas of the two oppositely-charged inks on the membrane surface enables increased partitioning of cations and anions within their preferred domains. This concept is demonstrated in Fig. 2b where the concentrations of cations and anions in the membrane are equal for all concentrations. While Donnan exclusion of co-ions occurs locally at the scale of the pattern, it does not occur on the scale of the membrane because both ions are attracted to an oppositely charged domain. For KCl, these electrostatic forces affect the cation and anion equally due to the equivalent magnitude of the charge on the ions. Thus, the constituent ions partition into the membrane at a stoichiometric ratio. For asymmetric salts, however, the electrostatic interactions affect the constituent ions disproportionately and skews the concentration of absorbed ions from the stoichiometry of the salt. Since the ions that comprise a salt must permeate through the membrane at a stoiciometric ratio, this suggests why the permeability of KCl is highest through the charge-patterned membrane.

Diffusion cell experiments were performed at varying KCl concentration to elucidates the mechanisms driving rapid KCl permeation of patterned membranes. The results are shown in Fig. 4. The single-charge membranes both show a monotonic increase in permeability with increasing KCl concentration (experimental results for other salts permeating through the single-charge membranes can be found in *ESI*, Fig. S6, but the trend is similar). This general trend is reinforced by the transport model (Fig. 2c). Furthermore, this behavior for the single-charge membranes is expected based on prior studies demonstrating reduced ionic resistance for exchange membranes at concentrations within the 1 mM to 100 mM range [14, 51]. Salt permeabilities for the charge-patterned mosaic membranes result, unexpectedly, in non-monotonic behavior. As KCl concentration is increased in the feed, permeability increases until c_b reaches 5 mM to 10 mM, then sharply reverses. Permeability values for the other salts decrease monotonically with increasing concentration (*ESI*, Fig. S7). Accounting for the local variation in electrostatic potential near

the solution-membrane interface, our model accurately predicts the divergence in $P(c_b)$ trends for single-charge membranes and charge-patterned membranes. Moreover, when using experimental estimates for the porosity, D_i, and χ terms, $P(c_b)$ for our model is in good quantitative agreement with experimental trends showing the decreasing P with c_b (*ESI*, Fig. S8). While we cannot explain the non-monotonicity observed for KCl within this model, it should be noted that this feature appears at a concentration where the Debye length becomes comparable to the pore size of the functionalized membranes (*i.e.*, 10 nm) [33]. Under these conditions, the concentration gradient across the membrane would be suppressed leading to reduced permeabilities. The theoretical framework we have developed can describe whether favorable ion partitioning, which leads to increased permeability, will occur, but cannot account for saturation effects that will result from ionic correlations and the interplay between pore size and Debye length.

Outside this, the trend for both types of membranes is the result of the influence of electrostatic interactions on the availability of ion species for transport. At large λ_D, electrostatic interactions are relatively strong. This causes both ionic species to favorably partition into charge-patterned membranes. Conversely, for single-charge membranes, co-ions (and therefore the whole salt) are excluded due to strong repulsion. At higher salt concentrations, and smaller λ_D, electrostatics are more effectively screened, and the permeability of the charged membranes collapses toward that of the uncharged membrane (Eq. 14 and Fig. 2). This perspective is reinforced by ion uptake experiments showing similar trends to the diffusion cell experiments (*ESI*, Fig. S9). The single-charge membranes had the highest uptake of its divalent counter-ion, the charge-patterned mosaic membranes had the highest uptake of KCl, and the uncharged membranes had significantly lower uptake compared to the charged membranes, with little to no variations between the salts. Donnan exclusion of a single-charge membrane's co-ion limits transport, but the electric double layer facilitates transport for a charge-patterned mosaic membrane.

In order to understand these trends for the charge-patterned membrane, it is imperative to consider the cross-talk between the two domains on the membrane surface. To aid in this interpretation, the electrostatic potential and local electric field were calculated from Eq. 13 and its derivatives. The results in the limit of thick ($\lambda_D >> L$) and thin ($\lambda_D << L$) Debye lengths are shown in Fig. 5. At high ionic strengths, $\lambda_D << L$, the magnitude of the electrostatic potential is low and drops off quickly from the membrane surface into the bulk solution. Along the x-direction, similarly rapid changes in the potential are observed as it transitions from a positive value to a negative value in a nearly step function-like manner at the interface between the oppositely-charged domains. The electric field lines that result from these variations in potential are superimposed on Fig. 5. For the case of thin Debye layers, the field lines are nearly

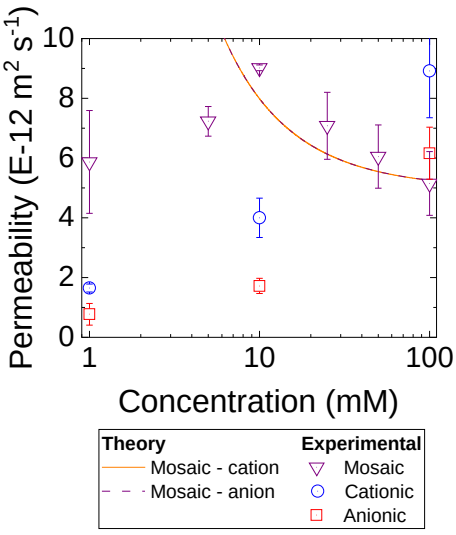

FIG. 4. Salt permeability as a function of salt concentration. The permeability was calculated from diffusion cell experiments with varying upstream salt concentrations. DI water was used as the downstream solution. The permeability of potassium chloride (KCl) through three different membrane types was characterized: membranes with a positively-charged surface (cationic), membranes with a negatively-charged surface (anionic), and membranes with charge-patterned surfaces (mosaic). The results for membranes with no surface charge (uncharged) are provided in *ESI*, Fig. S8. Error bars represent one standard deviation from the mean based on at least three membranes.

all vertical except in a region with a width on the order of λ_D near the interface between the domains. In this region, which is critical to salt transport through the charge-patterned mosaics, the field lines curve such that they originate at the surface of the positive domain and terminate at the surface of the negative domain. In this way, the repulsion of an ion by a like-charged region will cause the ion to travel along the electric field toward the oppositely-charged region. These results indicate that only ions very near the interface will be transported along the field lines towards the oppositely charged domain. Everywhere else, the ions will interact effectively with only a single domain (*ESI*, Fig. S10).

When the ionic strength of the solution is reduced and the value of λ_D increases, the cross-talk between domains grows considerably. The magnitude of the electrostatic potential is larger and it remains so over much greater distances. As such, the electric field lines drive ions away from the like-charged region to the oppositely charged region over far greater distances. Simply, at lower concentrations (larger λ_D), there exists a larger interfacial region relative to the width of the pattern stripes over which the differently-charged domains can interact with each other. This increased interaction between domains makes it more likely for ions to find an

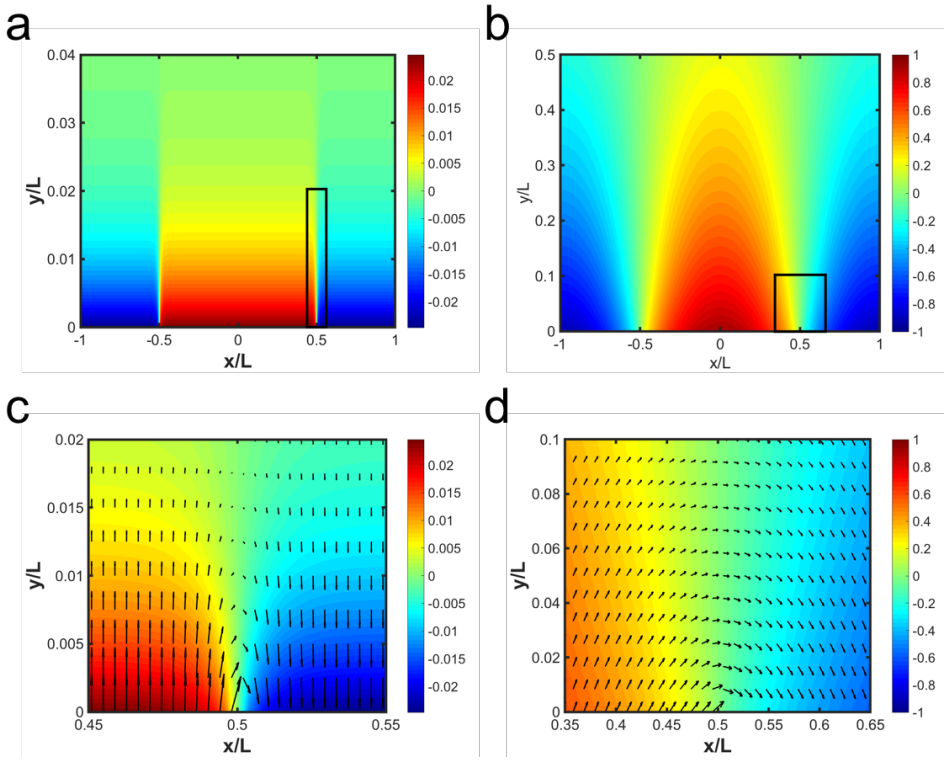

FIG. 5. Electrostatic potential (dimensionless; scaled by $\frac{4\sigma_0 L}{\pi\epsilon}$) and local electric field of a charge-patterned membrane. The electrostatic potential was calculated as a function of position using Eq. 13 and the local electric field was determined by taking the appropriate derivatives. Two limiting results are plotted: (a) Debye length, λ_D, much smaller than the stripe width, L, and (b) Debye length, λ_D, much larger than the stripe width, L. Panels (c) and (d) are magnified views of the regions indicated by the black boxes around the interface between the oppositely-charged domains at $x = \frac{L}{2}$ in panels (a) and (b), respectively.The arrows represent the magnitude and direction of the electric field lines. In these plots, the values of x and y are normalized by L. Please note that for the two limiting cases examined different scales are utilized to magnify the interfacial region between the oppositely-charged domains.

oppositely-charged region through which it can permeate the membrane (*ESI*, Fig. S10-S11). It is likely that this cross-talk between oppositely-charged domains over distances that scale as λ_D, and not transport limitations due to a mass transfer boundary layer, is why charge-patterned membranes with smaller domain sizes are seen to perform more effectively.

The preceeding discussion assumed a constant stripe width; and for a constant stripe width, higher concentrations (smaller λ_D) reduce both the communication between domains and the overall electrostatic interactions leading to weaker partitioning (*ESI*, Fig. S11). This reinforces the claim that ion partitioning is critical to the transport of salt (Fig. 2). The partition coefficient, plotted in Fig. 2a clearly demonstrates that for constant stripe widths (dashed lines) the partitioning of ions into the charge-patterned mosaic membrane sharply decreases and approaches the result of an uncharged membrane (*i.e.*, a value of 1) as the concentration in the upstream is increased and the Debye length decreases. The reduced partitioning, in turn, limits overall salt transport. This observation is consistent with our experimental results where higher bulk concentrations resulted in lowered salt transport for charge-patterned structures.

The effects of modifying the stripe width can also be considered. Subject to the constraints of the Debye–Hückel limit, decreasing L at constant values of λ_D (Fig. 2a, solid lines) causes the partitioning of cation and anions to sharply decreases from a value of approximately half that of the counter-ion partitioning for a single-charge membrane to a value of unity. In these cases, at smaller values of L, the magnitude of the electrostatic potential and, consequently, the driving force for ions to move toward their oppositely-charged region decreases; and as a result, partitioning decreases. Taken together, these results suggest that as techniques are developed to generate smaller pattern sizes a balance will need to be struck between maximizing cross-talk between domains, which is promoted by smaller pattern sizes, and exerting a sufficient electrostatic force to drive ions toward their oppositely-charged domain, which is favored by larger pattern sizes.

V. CONCLUSIONS

The experiments and analysis reported above demonstrate the ability for new transport mechanisms to emerge when multiple functionalities are patterned on a single membrane surface. This is highlighted most clearly by the divergent behavior of the single-charge and charge-patterned membranes. Despite the distinct behavior of each membrane type, the model developed above implies that it is the phenomenon of ion partitioning at the solution-membrane boundary that drives the observed trends. For the single-charge membranes, electrostatic repulsion restricts partitioning of the co-ions, thereby, limiting salt transport due to the need to maintain electroneutrality. For charge-patterned membranes, however, both cation and anions favorably partition into the membrane, facilitating salt transport. In its present form, the model does not account for the effects that arise when the Debye length becomes comparable to the pore size of the membrane [58]. As such, the model breaks down in this limit and resolving this issue will be the subject of future investigations. Regardless, knowledge of the cross-talk between charged domains within the double layer and the effect of the stripe width and λ_D on this cross-talk opens the possibility of patterning the surface functionality to strengthen interactions between the membrane and the solute of interest.

ACKNOWLEDGMENTS

Portions of this work were made possible with support from the National Science Foundation (NSF) through the Chemical and Biological Separations Program (Award Number: 1512089), and we appreciatively acknowledge this support. M.S. gratefully acknowledges support for this project from the Center of Environmental Science and Technology (CEST)/Bayer Predoctoral Fellowship at the University of Notre Dame and from National Water Research Institute/American Membrane Technology Association (NWRI-AMTA) Fellowship for Membrane Technology. S.J.S. gratefully acknowledges support from Notre Dame's Center for Nano Science and Technology Undergraduate Research Fellowship program. We would like to thank the center for Environmental Science and Technology at the University of Notre Dame (CEST) portions of this research were performed with instruments at this facility.

[1] Y. Zhang, J. L. Sargent, B. W. Boudouris and W. A. Phillip, *Journal of Applied Polymer Science*, 2015, **132**, 1–17.
[2] H. B. Park, J. Kamcev, L. M. Robeson, M. Elimelech and B. D. Freeman, *Science*, 2017, **356**, eaab0530.
[3] R. A. Segalman, *Materials Science and Engineering R: Reports*, 2005, **48**, 191–226.
[4] Z. Nie and E. Kumacheva, *Nature Materials*, 2008, **7**, 277–290.
[5] J. D. Ryckman, M. Liscidini, J. E. Sipe and S. M. Weiss, *Nano Letters*, 2011, **11**, 1857–1862.
[6] O. Heinz, M. Aghajani, A. R. Greenberg and Y. Ding, *Current Opinion in Chemical Engineering*, 2018, **20**, 1–12.
[7] B. V. Bhut, J. Weaver, A. R. Carter, S. R. Wickramasinghe and S. M. Husson, *Biotechnology and Bioengineering*, 2011, **108**, 2645–2653.
[8] Y. R. Smith, D. Bhattacharyya, T. Willhard and M. Misra, *Chemical Engineering Journal*, 2016, **296**, 102–111.
[9] J. L. Weidman, R. A. Mulvenna, B. W. Boudouris and W. A. Phillip, *Langmuir*, 2015, **31**, 11113–11123.
[10] J. L. Weidman, R. A. Mulvenna, B. W. Boudouris and W. A. Phillip, *ACS Applied Materials and Interfaces*, 2017, **9**, 19152–19160.
[11] M. L. Bruening, D. M. Dotzauer, P. Jain, L. Ouyang and G. L. Baker, *Langmuir*, 2008, **24**, 7663–7673.
[12] S. R. Lewis, S. Datta, M. Gui, E. L. Coker, F. E. Huggins, S. Daunert, L. Bachas and D. Bhattacharyya, *Proceedings of the National Academy of Sciences*, 2011, **108**, 8577–8582.
[13] M. a. C. Stuart, W. T. S. Huck, J. Genzer, M. Müller, C. Ober, M. Stamm, G. B. Sukhorukov, I. Szleifer, V. V. Tsukruk, M. Urban, F. Winnik, S. Zauscher, I. Luzinov and S. Minko, *Nature materials*, 2010, **9**, 101–13.
[14] G. M. Geise, M. a. Hickner and B. E. Logan, *ACS Applied Materials and Interfaces*, 2013, **5**, 10294–10301.
[15] I. Sadeghi, J. Kronenberg and A. Asatekin, *ACS Nano*, 2018, **12**, 95–108.
[16] A. O. W. Leung, N. S. Duzgoren-Aydin, K. C. Cheung and M. H. Wong, *Environmental Science & Technology*, 2008, **42**, 2674–2680.
[17] Y. Zhang, N. E. Almodovar-Arbelo, J. L. Weidman, D. S. Corti, B. W. Boudouris and W. A. Phillip, *npj Clean Water*, 2018, **1**, 1–14.
[18] T. J. Ward and K. D. Ward, *Analytical Chemistry*, 2012, **84**, 626–635.
[19] X. Jiang and Z. H. Fan, *Annual Review of Analytical Chemistry*, 2016, **9**, 203–222.
[20] J. Kamcev, M. Galizia, F. M. Benedetti, E.-S. Jang, D. R. Paul, B. D. Freeman and G. S. Manning, *Physical Chemistry Chemical Physics*, 2016, **18**, 6021–6031.
[21] G. S. Manning, *Annual Review of Physical Chemistry*, 1972, **23**, 117–140.
[22] G. S. Manning, *Accounts of Chemical Research*, 1979, **12**, 443–449.
[23] J. Kamcev, D. R. Paul and B. D. Freeman, *J. Mater. Chem. A*, 2017, **5**, 4638–4650.
[24] H. Yeager and A. Steck, *Journal of the Electrochemical Society*, 1981, **128**, 1880–1884.
[25] G. M. Geise, H. J. Cassady, D. R. Paul, B. E. Logan, M. A. Hickner, E. Logan and M. A. Hickner, *Phys. Chem. Chem. Phys.*, 2014, **16**, 21673–21681.

[26] J. Kamcev, D. R. Paul and B. D. Freeman, *Macromolecules*, 2015, **48**, 8011–8024.
[27] F. G. Helfferich, *Ion Exchange*, McGraw-Hill, 1962.
[28] G. M. Geise, B. D. Freeman and D. R. Paul, *Journal of Membrane Science*, 2013, **427**, 186–196.
[29] A. Yamauchi and T. Fukuda, *Annals of the New York Academy of Sciences*, 2003, **984**, 256–266.
[30] C. Cheng, A. Yaroshchuk and M. L. Bruening, *Langmuir : the ACS journal of surfaces and colloids*, 2013, **29**, 1885–92.
[31] A. M. Balachandra, J. Dai and M. L. Bruening, *Macromolecules*, 2002, **35**, 3171–3178.
[32] V. S. Rathee, S. Qu, W. A. Phillip and J. K. Whitmer, *Mol. Syst. Des. Eng.*, 2016, **1**, 301–312.
[33] P. Gao, A. Hunter, M. J. Summe and W. A. Phillip, *ACS Applied Materials and Interfaces*, 2016, **8**, 19772–19779.
[34] K. Söllner, *Biochemische Zeitschr*, 1932, **244**, 370–381.
[35] R. Neihof and K. Sollner, *The Journal of Physical and Colloid Chemistry*, 1950, **54**, 157–176.
[36] Y. Chen, Y. Cui, Y. Jia, K. Zhan, H. Zhang, G. Chen, Y. Yang, M. Wu and H. Ni, *Journal of Applied Polymer Science*, 2014, **131**, n/a–n/a.
[37] T. Fujimoto, K. Ohkoshi, Y. Miyaki and M. Nagasawa, *Science (New York, N.Y.)*, 1984, **224**, 74–76.
[38] S. Qu, Y. Shi, S. Benavides, A. Hunter, H. Gao and W. A. Phillip, *Chemistry of Materials*, 2017, **29**, 762–772.
[39] T. Fukuda, W. Yang and A. Yamauchi, *Journal of Membrane Science*, 2003, **212**, 255–261.
[40] J. N. Weinstein and S. R. Caplan, *Science (New York, N.Y.)*, 1968, **161**, 70–72.
[41] J. N. Weinstein and S. R. Caplan, *Science (New York, N.Y.)*, 1970, **169**, 296–298.
[42] M. Higa, D. Masuda, E. Kobayashi, M. Nishimura, Y. Sugio, T. Kusudou and N. Fujiwara, *Journal of Membrane Science*, 2008, **310**, 466–473.
[43] M. Higa, M. Kobayashi, Y. Kakihana, A. Jikihara and N. Fujiwara, *Journal of Membrane Science*, 2013, **428**, 267–274.
[44] S. Rajesh, Y. Yan, H.-C. Chang, H. Gao and W. A. Phillip, *ACS nano*, 2014, **8**, 12338–45.
[45] B. Bolto, M. Hoang and T. Tran, *Desalination*, 2010, **254**, 1–5.
[46] P. Gao, A. Hunter, S. Benavides, M. J. Summe, F. Gao and W. A. Phillip, *ACS Applied Materials & Interfaces*, 2016, **8**, 3386–3395.
[47] F. G. Donnan, *Chemical Reviews*, 1924, **1**, 73–90.
[48] F. G. Donnan, *Journal of Membrane Science*, 1995, **100**, 45–55.
[49] J. S. Mackie and P. Meares, *Proceedings of the Royal Society A: Mathematical, Physical and Engineering Sciences*, 1955, **232**, 498–509.
[50] G. M. Geise, B. D. Freeman and D. R. Paul, *Journal of Membrane Science*, 2012, **423**, 195–208.
[51] P. Długołecki, B. Anet, S. J. Metz, K. Nijmeijer and M. Wessling, *Journal of Membrane Science*, 2010, **346**, 163–171.
[52] A. E. Yaroshchuk, *Advances in Colloid and Interface Science*, 2008, **139**, 150–173.
[53] H. Ohshima and S. Ohki, 1985, **47**, 673–678.
[54] W. E. Boyce, R. C. DiPrima and D. B. Meade, *Elementary Differential Equations and Boundary Value Problems*, Wiley, 11th edn, 2017.
[55] E. L. Cussler and E. L. Cussler, *Diffusion: Mass Transfer in Fluid Systems*, Cambridge University Press, 1997.
[56] G. S. Manning, *Quarterly reviews of biophysics*, 1978, **11**, 179–246.
[57] S. U. Hong, R. Malaisamy and M. L. Bruening, *Journal of Membrane Science*, 2006, **283**, 366–372.
[58] Y. Yan, L. Wang, J. Xue and H. C. Chang, *Journal of Chemical Physics*, 2013, **138**, year.

TOC Graphic and summary:

Charge-patterned mosaic membranes exhibit salt permeabilities that increase with decreasing concentration, which is opposite of the trend observed for single charge membranes.